

Geothermal heating in the Panama Basin. Part II: abyssal water mass transformation

D. Banyte¹, M. Morales Maqueda¹, D. A. Smeed³, A. Megann³, R. Hobbs², S. Recalde⁴

¹School of Marine Science and Technology, Newcastle University, Newcastle, UK

²Department of Earth Sciences, Durham University, Durham, UK

³National Oceanography Centre, Southampton, UK

⁴Instituto Oceanográfico de la Armada, Guayaquil, Ecuador

Key Points:

- Geothermal heating is the strongest water mass transformation process for abyssal waters inside the Panama Basin.
- Almost all abyssal water mass transformation occurs within the weakly stratified bottom boundary layer (wsBBL) hundreds of meters thick.
- The thickness of the wsBBL may be used to differentiate the basin walls from the basin bottom.

Corresponding author: Donata Banyte, donata.banyte@newcastle.ac.uk

Abstract

Diabatic upwelling of abyssal waters is investigated in the Panama Basin employing the water mass transformation framework of *Walín* [1982]. We find that, in large areas of the basin, the bottom boundary layer is very weakly stratified and extends hundreds of meters above the sea floor. Within the weakly stratified bottom boundary layer (wsBBL) neutral density layers intercept the bottom of the basin. The area of these density layer incrops increases gradually as the abyssal waters become lighter. Large incrop areas are associated with strong diabatic upwelling of abyssal water, geothermal heating being the largest buoyancy source. While almost half of all water mass transformation is due to extreme turbulence downstream the Ecuador Trench, the only abyssal water inflow passage, inside the basin, water mass transformation is accomplished almost entirely by geothermal heating.

1 Introduction

The diabatic upwelling of abyssal waters is arguably the least well understood part of the meridional overturning circulation. Introduced by *Stommel* [1958], the picture of a homogeneous, widespread upwelling driven by turbulent mixing with an average diffusivity of $10^{-4} \text{ m}^2 \text{ s}^{-1}$ [*Munk*, 1966] was challenged by direct measurements of the deep turbulent dissipation [*Polzin et al.*, 1997]. Deep ocean turbulence turns out to be highly inhomogeneous: at least an order of magnitude larger than the canonical estimate of *Munk* [1966] in narrow passages and canyons, and over rough bathymetry, but an order of magnitude smaller in most of the rest of the ocean. Consequently, there is a prevailing notion that the bulk of the abyssal water upwelling occurs in localized regions of complex and rough bathymetry.

In recent years, however, it has been argued that bottom intensified mixing could lead to deep waters becoming denser, rather than lighter, and therefore to diabatic downwelling, rather than upwelling [*Klocker and McDougall*, 2010; *de Lavergne et al.*, 2016; *Ferrari et al.*, 2016]. The density flux due to diapycnal mixing is commonly parametrized as $K^z \gamma_z$, where K^z is the vertical turbulent diffusivity and γ_z is the vertical density gradient. In the deep ocean, stratification rapidly increases upwards. Thus, if turbulent diffusivity were uniform in the vertical, the stronger density flux at lighter densities would cause density flux divergence, i.e., buoyancy convergence, or diabatic upwelling. However, observations show that turbulent kinetic energy (TKE) dissipation can rapidly increase with depth above rough bathymetry [e.g., *Ledwell et al.*, 2000]. Assuming that the turbulent density flux varies similarly to TKE in the vertical, this could lead to a density flux convergence and, consequently, to diabatic downwelling. A conundrum arises in the observation that vast areas of the deep ocean have favourable conditions for diabatic upwelling to occur, but turbulent mixing is too weak there (small K^z) to generate as much diabatic upwelling of abyssal waters as we know is needed to support the global meridional overturning circulation. At the same time, regions of intense and bottom intensified turbulent mixing imply diabatic downwelling, instead of upwelling.

Several solutions have been suggested to solve this puzzle. *Klocker and McDougall* [2010] observed that, since the area of ocean basins decreases with depth, the net (integrated) density flow across a given isopycnal of area S_0 can still be larger than the flux across a deeper isopycnal of area S_1 , even if K_z increases with depth, resulting in density flux divergence over the bounded density layer or diabatic upwelling. Following *Jackett and McDougall* [1997], we define an isopycnal as a surface of neutral density γ , where we subtract 1000 kg m^{-3} from the neutral density values. The difference between the two density surface areas, $S_0 - S_1$, is called the density layer intercept with the bottom of the basin. It has been hypothesised that abyssal water upwelling happens along the bottom boundaries of the basin, and is predominantly set by the size of the bottom intercept ar-

eas of the density layers [Ferrari *et al.*, 2016; de Lavergne *et al.*, 2016; McDougall and Ferrari, 2017].

Geothermal heating, acting solely at the bottom boundary, contributes to buoyancy flux convergence within the weakly stratified Bottom Boundary Layer (wsBBL). Modelling studies of various levels of complexity [e.g., Adcroft *et al.*, 2001; Emile-Geay and Madec, 2009; Hofmann and Morales Maqueda, 2009] have debated the importance of geothermal heating for watermass transformation with simulated contributions ranging from negligible to over 30%. The single observational estimate, de Lavergne *et al.* [2016], finds a 40% contribution of geothermal heating to the upwelling of the Antarctic Bottom Waters (AABW).

The purpose of this study is to compare new observational evidence with the developing theories on abyssal water mass transformation. We investigate the semi-enclosed Panama Basin using recently collected high-resolution hydrographic data. We adopt the water mass transformation framework of Walin [1982], as explained in section 3, to evaluate the importance of geothermal heating for abyssal water diapycnal upwelling (section 4).

2 The Panama Basin

The Panama Basin is almost completely shielded from the rest of the equatorial Pacific Ocean below about 2500 m (Figure 1). The only deep water exchange pathway is a passage between the Carnegie Ridge and the South American continental slope called the Ecuador Trench, with a sill depth of about 2930 m. An inflow through the trench into the basin at a rate of 0.29 ± 0.07 Sv with neutral density range between 28.016 kg m^{-3} and 27.967 kg m^{-3} was estimated in the first part of this study [Banyte *et al.*, 2018a]. In this study, we show that the discretized density layer $\gamma = 27.970 \pm 0.001 \text{ kg m}^{-3}$ has the largest incrop area that results in largest water mass transformation rate in the wsBBL driven by the geothermal heating. As a result, we identify the isopycnal $\gamma_{27.970}$ as the upper boundary of the abyssal water layer.

Hydrography reveals that abyssal waters entering the basin experience a strong transformation in the first 200 km downstream of the inflow [Banyte *et al.*, 2018a]. Over this short distance, all waters denser than 27.988 kg m^{-3} are transformed into lighter waters. The observed bottom density change of 0.028 kg m^{-3} is also reflected in a bottom temperature rise of 0.15°C . Banyte *et al.* [2018a] hypothesised that the intense turbulent mixing leading to this dramatic water mass transformation is caused by a hydraulic jump resulting from critical flow through the passage. Abyssal water mass transformation further into the basin is much more gradual, but comparable in magnitude, and is estimated to be 0.021 kg m^{-3} (0.10°C).

3 Theory: Abyssal Water Transformation

Abyssal water mass transformation inside the basin is analysed using the water mass transformation framework of Walin [1982] assuming steady state conditions for a volume of fluid, ΔV , bound by neutral density surfaces, γ and $\gamma + \Delta\gamma$. In general, we follow the notation of Nurser *et al.* [1999] and use their derivation of volume and mass conservation for the volume of fluid. The lateral flux of fluid into ΔV is denoted by $\Delta\Psi$, the diabatic flows (water mass transformation) through the bounding density surfaces are denoted by $G(\gamma)$ and $G(\gamma + \Delta\gamma)$ (Figure 2). The analysis makes the approximation that all density transformations are due to either geothermal heatfluxes or turbulent mixing, neglecting the effects of cabbeling, thermobaricity, and neutral helicity. Unlike Nurser *et al.* [1999], however, $G(\gamma)$ is chosen to be positive in the direction of decreasing density (or decreasing depth). Thus, by this definition, water mass transformation leading to lighter water is positive ($G(\gamma) > 0$):

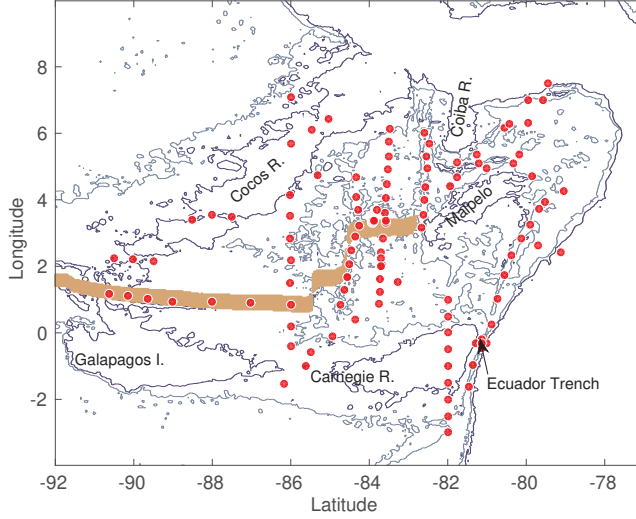


Figure 1. The bathymetry of the Panama Basin. Red dots indicate the locations of CTD casts collected between December 2014 and March 2015. Bathymetry contours mark the depths of 2000 m and 3000 m. The thick, brown line marks the location of geothermal heating larger than 500 mW m^{-2} .

$$G(\gamma) = \frac{\partial D_{diff}(\gamma)}{\partial \gamma} + \frac{\partial D_{surf}(\gamma)}{\partial \gamma}, \quad (1)$$

where D_{diff} is the net turbulent density flux across isopycnal γ , positive in the direction of increasing densities, and D_{surf} is the surface density outflux through the seabed of all the water denser than γ and is caused by geothermal heating.

Equation 1 links the rate of water mass transformation to the processes causing the said transformation. A diapycnal volume flux directed from dense to light water $G(\gamma) > 0$ requires a divergence of density fluxes driven either by turbulence, $\partial D_{diff}/\partial \gamma > 0$, or by geothermal heating, $\partial D_{surf}/\partial \gamma > 0$.

The integrated downgradient diffusive density flux across the isopycnal γ of area $S_D(\gamma)$ can be expressed as

$$D_{diff}(\gamma) = - \langle F(\gamma) \rangle S_D(\gamma), \quad (2)$$

where $F(\gamma)$ is upgradient density flux that is sometimes parametrized through diapycnal vertical diffusivity K^z and density gradient γ_z as: $F(\gamma) = -K^z \gamma_z$, with z increasing downwards. The density fluxes in equation 2 are averaged over the whole isopycnal as:

$$\langle F(\gamma) \rangle = \frac{1}{S_D(\gamma)} \int_{S_D(\gamma)} F dS_D. \quad (3)$$

Similarly, $D_{surf}(\gamma)$ can be expressed as

$$D_{surf}(\gamma) = -\frac{\alpha}{C_p} \langle q(\gamma) \rangle S_F(\gamma), \quad (4)$$

where α is the thermal expansion coefficient of seawater and C_p is the heat capacity of seawater. Both are considered to be constant. $\langle q(\gamma) \rangle$ is the average geothermal heatflux over the sea floor region of area $S_F(\gamma)$ located underneath isopycnal γ :

$$\langle q(\gamma) \rangle = \frac{1}{S_F(\gamma)} \int_{S_F(\gamma)} q dS_F, \quad (5)$$

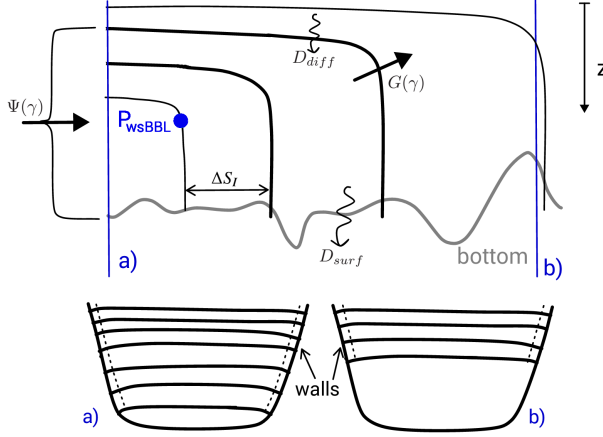


Figure 2. Schematics of discretized density layers in an idealised basin along meridional transect (top) and two zonal transects: near to the source (a) and further into the basin (b). The net inflow into the basin between the seabed and the isopycnal layer γ is denoted by $\Psi(\gamma)$. Similarly, $G(\gamma)$ denotes the net water mass transformation rate across the density surface γ . Diffusive and geothermal density fluxes are marked by D_{diff} and D_{surf} . The top figure visualizes formation of incrops with the area of ΔS_I , while zonal transects below - formation of bottom intercept areas at the sloping walls of the basin.

where q is the in-situ geothermal heatflux.

Introducing (2) and (4) in (1), we reach the following expression.

$$\begin{aligned} G(\gamma) &= g_{dF} + g_{dq} + g_F + g_q = \\ &= - \left(\frac{\partial F(\gamma)}{\partial \gamma} + \frac{\alpha}{C_p} \frac{\partial q}{\partial \gamma} \right) S - \left(F(\gamma) + \frac{\alpha}{C_p} q \right) \frac{\partial S}{\partial \gamma}, \end{aligned} \quad (6)$$

where, for convenience, we have dropped the angle brackets from the average quantities defined in (3) and (5). We have also made the approximation $S_D \simeq S_F = S$.

The $\partial S / \partial \gamma$ is always negative, because horizontal area of isopycnals is increasing with lighter densities located higher up in the water column. The increase in S happens due to the access of lighter waters to the boundary, either the bottom of the basin, or its walls (Figure 2). Hence, $\partial S / \partial \gamma$ denotes the bottom intercept area, which is a sum of incrop area at the bottom of the basin and bottom intercepts at the basin walls.

As $\partial S / \partial \gamma$ is negative, the terms g_F and g_q in equation 6 are always positive. The term g_{dq} , which represents spatial variation of geothermal heating, we show, is also positive in the Panama Basin. The only negative term in equation 6 is expected to be g_{dF} on the condition that density fluxes F are bottom intensified.

In the steady state, if there is inflow of abyssal water into the basin, the integrated volume flux between the seabed and isopycnal γ ($\Psi(\gamma)$) increases monotonically approaching the upper boundary of the inflow, above which the flow reverses, and so must $G(\gamma)$. In other words, the net water mass transformation through the sequence of isopycnals increases as water becomes lighter. This increase must be associated with a concomitant increase in at least one of the terms of the decomposition in equation 6. We will argue below that the terms growing the fastest with decreasing γ are those proportional to $\partial S / \partial \gamma$, namely the terms g_F and g_q . This study, consistent with the global analysis of [de Lavergne et al., 2016], shows that lighter abyssal waters tend to have larger bottom inter-

cept areas, typically reaching a maximum for the density range corresponding to the upper boundary of abyssal waters.

4 Observations

4.1 Data description

All observational data used in this study were collected between December 2014 and March 2015. The two cruises on RRS James Cook (JC112) and FS Sonne (SO238) were funded as part of the multi-institute research project OSCAR (Oceanographic and Seismic Characterisation of heat dissipation and alteration by hydrothermal fluids at an Axial Ridge) that aims to investigate the coupling of hydrothermal flow between the ocean and the lithosphere and its impact on the evolution of the oceanic crust and on basin-scale circulation. All of the 132 conductivity-temperature-depth (CTD) casts went down to approximately 5 m above the bottom. The vertical distributions of temperature, salinity, and dissolved oxygen were measured with a SBE911plus CTD system (Sea-Bird Electronics, Inc.). The accuracy of the sensors was 0.001°C , 0.0003 S m^{-1} , 1 dB , and 0.1 ml l^{-1} ($4.47 \mu\text{mol kg}^{-1}$) for temperature, conductivity, pressure, and oxygen, respectively. This results in density accuracy of 0.004 kg m^{-3} . However, the precision of CTD sensors is much greater than their accuracy, which allows us to accurately evaluate density gradients as small as $10^{-5} \text{ kg m}^{-4}$ when defining the upper boundary of the wsBBL. The use of density gradient criteria to identify the wsBBL is discussed further in [Banyte *et al.*, 2018b].

The geothermal heatflux in the basin was estimated by using the age map of the ocean floor [Müller *et al.*, 1997] as a proxy for the heat flow. This sea floor age dataset has a resolution of $0.1^{\circ} \times 0.1^{\circ}$. Then, we applied the formula of Stein and Stein [1992] linking the age of the bedrock to the heat flow through the crust: $q(t) = 510t^{-0.5}$, where t is crust age in Myr (million years) and q is the heat flow in mWm^{-2} . The ridges traversing the western side of the Basin stand out due to their large heat flow estimate (Figure 1). It is expected that the Stein and Stein [1992] formula overestimates the geothermal heatflux for very young crust, as their estimate in that case approaches infinity. Hence, we imposed an upper limit of 550 mW m^{-2} on the geothermal heating estimates. The resulting difference in the total heatflux for the incrop of the $\gamma = 27.970 \pm 0.001 \text{ kg m}^{-3}$ layer is estimated to be 4%.

4.2 The weakly stratified bottom boundary layer

To define the boundaries of the bottom intercept areas of density layers, the bottom densities of abyssal waters must be mapped. However, a near bottom density measurement might not represent abyssal waters if taken over shallow locations. Instead, the hydrographic data indicate that a thick wsBBL covers most of the basin (Figure 3). Assuming that thick wsBBL can only form at the bottom of the basin, but not over basin walls, such as shallow ridges, only profiles having a thick wsBBL were taken to map the bottom density.

The wsBBL was defined as the abyssal region where density gradients are smaller than $1 \times 10^{-5} \text{ kg m}^{-4}$ (see details in Appendix .1), computed over 50 m depth intervals. For this reason only stations with the estimated wsBBL thickness larger than 50 m were used for mapping. Of the 132 neutral density profiles in the Panama Basin, 78 had wsBBLs thicker than 50 m and, for these profiles, the median thickness of the wsBBL is 350 m; at seven sites the wsBBL was found to be over 1000 m thick.

The density and pressure, γ_{wsBBL} and P_{wsBBL} , at the upper boundary of the weakly stratified bottom waters are highly correlated with one another (top right panel of Figure 3) and vary smoothly in space. This is a common property of abyssal waters observed

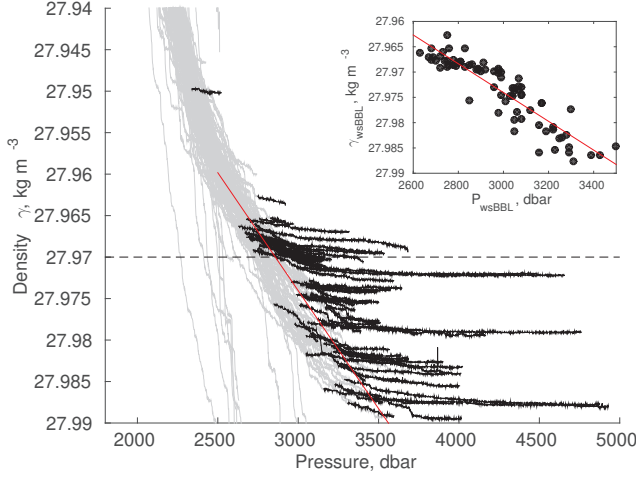


Figure 3. Vertical neutral density profiles (grey) with the wsBBL, identified by the search algorithm presented in Appendix .1, marked in black. The horizontal dashed line marks the upper boundary of abyssal waters. The top right figure shows the density-pressure relation estimated at the top of wsBBL with their linear fit marked by the red line.

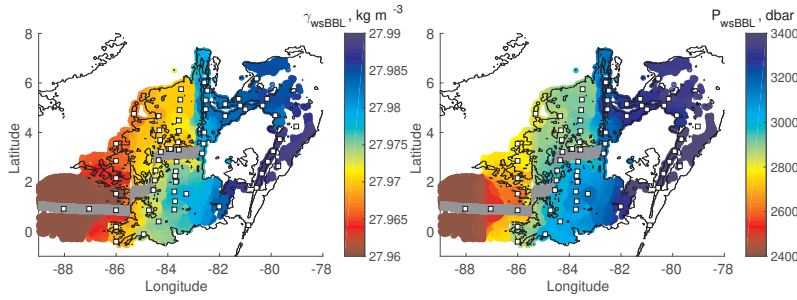


Figure 4. Map of interpolated γ_{wsBBL} (left) and recomputed P_{wsBBL} (right). The squares indicate the location of the CTD casts. The thin black line delineates the 2900 m isobath, which approximately corresponds to the $P_{wsBBL}(\gamma = 27.970)$ value. The thick grey line indicates the location of the spreading axial ridges in the basin.

over most of the global ocean basins [Banyte *et al.*, 2018b]. Consequently we use γ_{wsBBL} to map bottom density and the linear relation between γ_{wsBBL} and P_{wsBBL} to outline shallow bathymetry (Figure 4) with details given in Appendix .2.

Taking the bathymetry into account, the density map reveals the pathway of abyssal waters as they fill the basin. The densest waters, as expected, are channelled along the deepest trenches in the eastern part of the basin. However, as they fill the basin, the bottom waters become lighter, and their P_{wsBBL} becomes shallower, which leads to weaker topographic constraints. In the east of the basin, the narrow trenches are the main arteries along which the dense water spreads. In the west, the similarly narrow trenches are completely flooded with nearly homogeneous bottom waters, the upper boundary of which is located some 800 m higher up in the water column (Figure 3). Overall, shallow P_{wsBBL} supports wsBBLs that can become over 1000 m thick over deep trenches.

4.3 Incrops

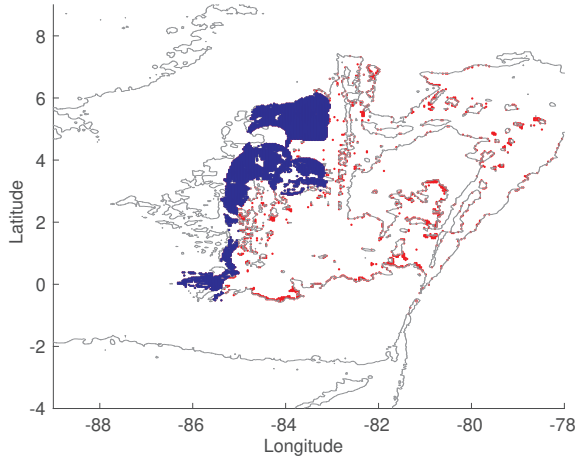
The term incrop was used by *de Lavergne et al.* [2016] to refer to the bottom intercept area of ocean density layers, by analogy with the density layer outcrops at the sea surface. In the same way as outcrops at the sea surface can be associated with mixed layers hundreds of meters deep, incrops can result in equally thick wsBBLs along the abyssal water spreading path. However, nearly flat isopycnals can be interrupted by sloping bathymetry along continental slopes, oceanic ridges, and sea mounts, creating thin wsBBLs just a few meters thick, as observed for example on the continental slopes [e.g., *Moum et al.*, 2004]. We call the latter regions the walls of the basin.

In this study, only profiles with wsBBL thicker than 50 m were used for bottom density interpolation, hence, shallower density-depth profiles were therefore omitted from the interpolation. The resulting bottom density map reflects the map of incrops - bottom intercept areas of discretized density layers that are allowed to have thick wsBBL if only bathymetry permitted it. At the same time, the bottom intercept areas at the sloping walls of the basin cannot be directly observed either from our data or from historical datasets, because most of the CTD profiles stop at least 5 m above the bottom. Instead, such areas are inferred from maps of stratification and bathymetry by assuming flat γ_{wsBBL} surfaces at the depth of P_{wsBBL} . In this way, the map of incrops as shown in Figure 4 can be completed with the bottom intercept areas at the basin walls (details in Appendix .2).

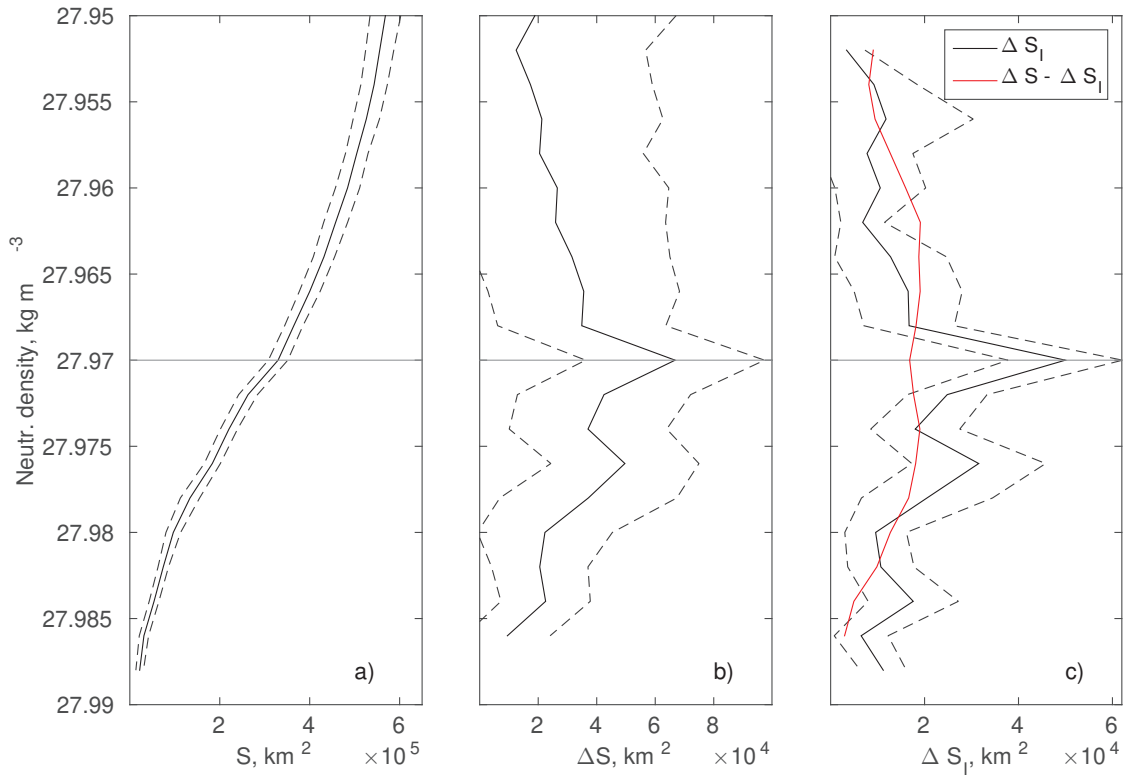
In the Panama Basin, the density layer $\gamma = 27.970 \pm 0.001 \text{ kg m}^{-3}$ is estimated to have the largest incrop area: about 75% of the total bottom intercept area is estimated to reside over the western side of the basin, where this density layer intercepts the bottom of the basin, while the remaining 25% of the bottom intercept is located away from the incrop, along the continental slopes and the flanks of shallow ridges (Figure 5). However, while isopycnal $\gamma_{27.970}$ has the largest incrop area, the lighter isopycnal $\gamma_{27.950}$ finishes to fill the bottom of the basin. This means that all of the lighter density layers do not form incrops with thick wsBBL, but have bottom intercept areas at the walls of the basin forming very thin wsBBLs (less than 50 m thick). In this study, waters with densities higher than $\gamma = 27.970 \text{ kg m}^{-3}$ are referred to as the abyssal water layer.

For abyssal waters, incrop areas tend to be larger for lighter densities (Figure 6c), reaching a maximum for the upper boundary of abyssal waters at $\gamma_{27.970}$. The bottom intercept areas at the basin walls are also slightly increasing with lighter waters, but less sharply than incrops. Furthermore, for most of the lighter abyssal waters, the areas of the bottom intercepts at the walls are smaller than the incrop areas for the same density layers. Therefore, although the total area of density layers is monotonically increasing as waters become lighter (Figure 6a), this does not mean that hypsometry (increase in the area of the ocean basins with depth) defines the size of the bottom intercept areas for the abyssal waters in the basin.

The spatial extent of abyssal isopycnals is strongly controlled by transformation processes which prevent them from spreading uniformly through the basin (Figure 4). It is instructive to estimate the hypothetical intercept area of the abyssal waters in the basin if they could spread horizontally without transformation to fill the basin. In this case, the intercept area would be controlled purely by the basin average stratification and by hypsometry. We have done this calculation using the $P_{wsBBL} - \gamma_{wsBBL}$ relation discussed above (Figure 7). Bathymetry by itself would allow larger spatial extents of all abyssal waters up to the isopycnal $\gamma_{27.950}$, with the largest differences estimated below $\gamma_{27.970}$ isopycnal. Hence, the area of abyssal waters is controlled not by hypsometry but by the existence and extent of incrops.



277 **Figure 5.** Spatial distribution of the largest incrop, corresponding to the neutral density layer $\gamma =$
 278 $27.970 \pm 0.001 \text{ kg m}^{-3}$. Blue dots mark the incrop area ΔS_I , while the red dots mark the rest of the total
 279 bottom intercept area ($\Delta S - \Delta S_I$). Bathymetry contours mark the depth of 3000 m.



280 **Figure 6.** a) Surface area of the neutral density surfaces, b) bottom intercept area of the discretized density
 281 layers, and c) incrop area with the red line representing the bottom intercepts at the walls of the basin. Both
 282 b) and c) are calculate for a density increment of 0.002 kg m^{-3} . Dashed lines show ranges of error estimates
 283 caused by the sparse sampling of the basin. The horizontal line marks the upper boundary of abyssal waters.

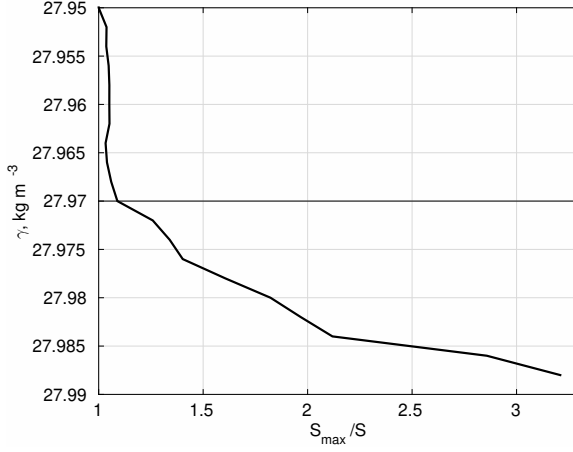


Figure 7. Ratio of the maximal area of a density layer allowed by hypsometry to the observed area: $S_{max}(\gamma)/S(\gamma)$.

4.4 Geothermal heating contribution to water mass transformation

In a semi-enclosed basin, such as the Panama Basin, and assuming a steady state, volume conservation dictates that integrated abyssal water volume influx into the basin $\Psi(\gamma)$ is equal to water mass transformation across the abyssal water boundary γ . Hence, the isopycnal corresponding to the lightest abyssal waters that inflow into the Panama Basin through the Ecuador Trench passage will experience the largest diapycnal upwelling. They also happen to have the largest incrop area, as was shown above. Both turbulent diffusion and geothermal heating contribute to density flux divergence over the incrops (the terms g_F and g_q in equation 6 are always positive). In this section, we evaluate the contribution of geothermal heating to abyssal water mass transformation.

Geothermal heating in the Panama Basin is highly variable in space. The three spreading ridges on the western side of the basin emit large geothermal heat fluxes (Figure 1) in comparison to the basin average flux of 210 mW m^{-2} . Yet, while heat fluxes directly over the ridges have in all likelihood an important effect on the local circulation, the incrop areas of lightest abyssal waters extend well beyond the ridges, which suggests that the contribution of geothermal hotspots to the total density flux divergence over the incrops is modest. For example, approximately 2% of the total bottom intercept area of the isopycnal $27.970 \pm 0.001 \text{ kg m}^{-3}$ is located above geothermal sources larger than 550 mW m^{-2} , contributing only 10% to the total water mass transformation associated with geothermal heating in this layer.

As spreading ridges are located on the western side of the basin, the average geothermal heating q enveloped by lighter densities is increasing, $\partial q / \partial \gamma < 0$ (Figure 8). Respectively, the term g_{dq} in equation 6 is positive. For abyssal waters, the estimated average density gradient of q is of the order of 5 W m kg^{-1} . Due to large incrop areas, abyssal waters have exceptionally small ratios of isopycnal surface area, S , to bottom intercept area, ΔS , which we show in the section below to be ~ 5 for density layers with $\Delta \gamma = 0.002 \text{ kg m}^{-3}$ increments. As a result, a comparison of terms g_{dq} and g_q reveals that g_{dq} is $\sim 25\%$ of g_q and has a non-negligible contribution to the abyssal water upwelling.

The lightest abyssal water layer $27.970 \pm 0.001 \text{ kg m}^{-3}$ has the largest bottom intercept area and receives the largest amount of geothermal heat at around $(1.7 \pm 0.6) \times 10^{10} \text{ W}$ (Figure 8); the error analysis for this estimate is presented in Appendix .2. This geother-

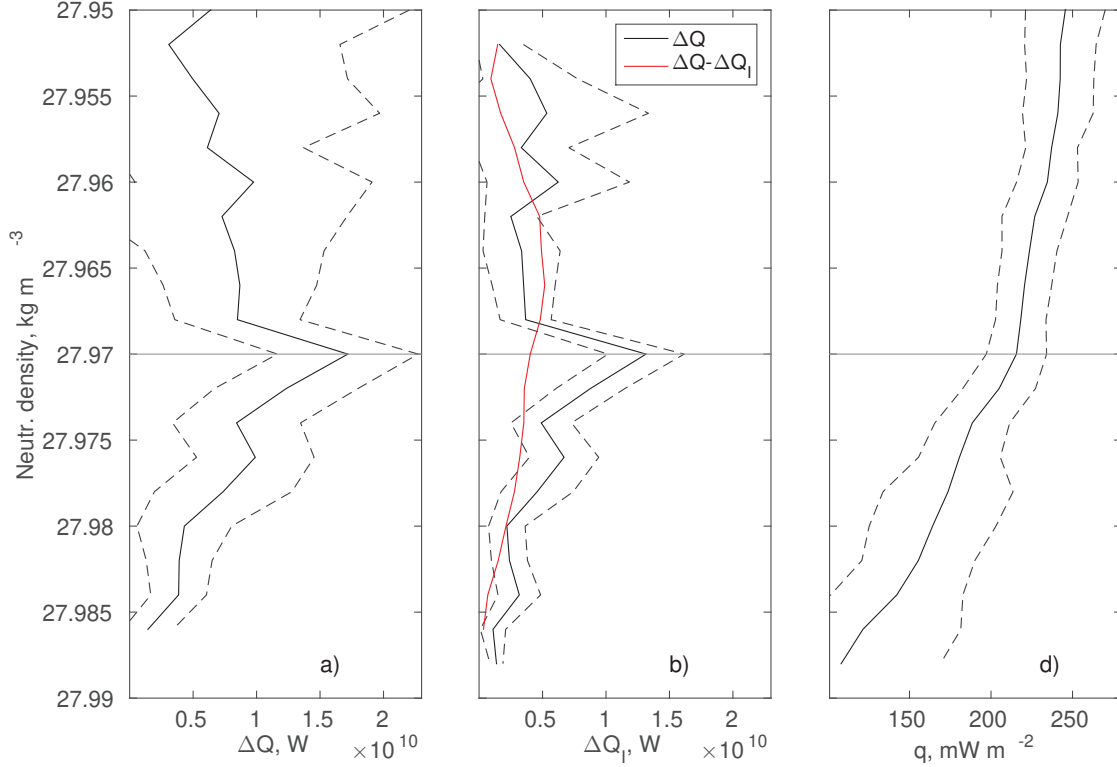


Figure 8. a) Geothermal heat flux over the total bottom intercept area of an isopycnal layer, b) geothermal heatflux only over the incrop with the red line representing geothermal heat gain at the walls of the basin, and c) average geothermal heat flux over the entire area covered by an isopycnal. All are calculate for a density increment of 0.002 kg m^{-3} . Dashed lines show ranges of error estimates caused by the sparse sampling of the basin. The horizontal line marks the upper boundary of abyssal waters.

mal heating is associated with an estimated abyssal water upwelling of $g_q = 0.32 \pm 0.11 \text{ Sv}$ across the density surface $\gamma_{27.97}$. These calculations have been made with a thermal expansion coefficient of $\alpha = (1.5 \pm 0.15) \times 10^{-4} \text{ K}^{-1}$ and a heat capacity of seawater of $C_p = 3992 \text{ J kg}^{-1} \text{ K}^{-1}$. Since the abyssal water inflow into the basin is $0.29 \pm 0.07 \text{ Sv}$ [Banyte *et al.*, 2018a], these estimates show that geothermal heating is the dominant process causing water mass transformation in the basin (from 60% to 100%), when away from the highly turbulent region of the Ecuador trench.

In conclusion, the abyssal water upwelling in the Panama Basin is strong both due to the strong geothermal heating, which is estimated to be three times the global average, but also due to spatial distribution of geothermal hotspots located at the far-end from the abyssal water inflow passage.

4.5 The influence of stratification on water mass transformation

Observations show that turbulent energy dissipation can increase by at least an order of magnitude over areas of rough topography [e.g., Waterhouse *et al.*, 2014]. The bottom intensification of mixing is only modest over smooth sea floors. Away from the boundaries, the ocean seems to have a more or less uniform background diffusivity of $K_b^z = 10^{-5} \text{ m}^2 \text{ s}^{-1}$. This raises the question of how this small background diffusivity affects the abyssal and deep water upwelling in the Panama Basin. Here, we investigate whether interior water upwelling driven by constant turbulent diffusivity in an environment

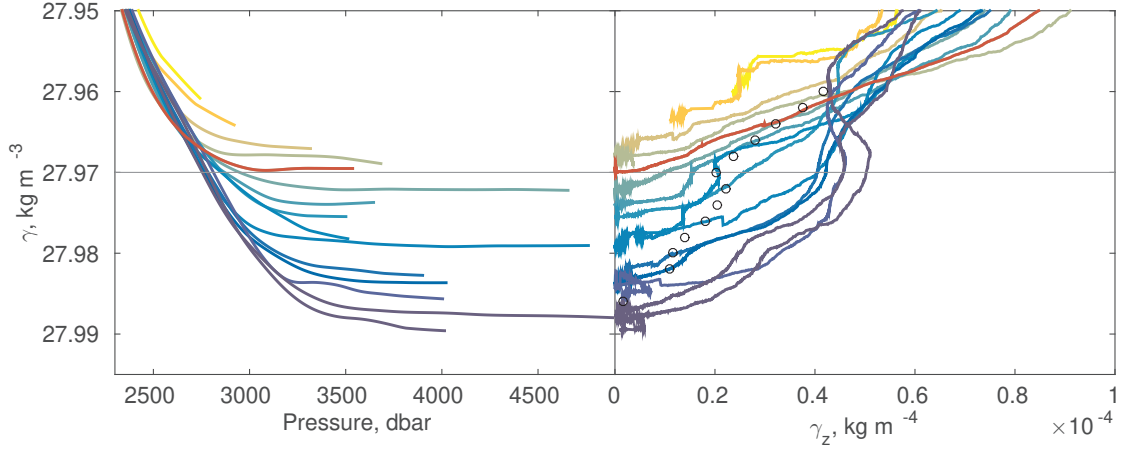


Figure 9. Average density-pressure (left) and density gradient profiles (right) over the incrops discretized with density increments of 0.002 kg m^{-3} . The red profile represents the average profile located over the largest incrop area of $\gamma_{27.97}$. The horizontal line marks the upper boundary of abyssal waters.

where stratification increases rapidly above the wsBBL can be significant in comparison to water upwelling at the boundaries.

The total surface area of density layers (S) is significantly larger than the size of their bottom intercept areas (ΔS), especially for waters lying above the abyssal water layer. Stratification increases with height above the bottom, which with a large surface area of isopycnals, could dominate the vertical divergence of the turbulent density flux and, correspondingly, the diabatic upwelling in the basin's interior. For the case of weak background diffusivity, taken as a constant for both basin's interior and at the upper boundary of the wsBBL, the terms g_{dF} and g_F in equation 6 can be compared. In this case, density fluxes are parametrized as $F(\gamma) = K_b^z \gamma_z$.

Comparing terms g_{dF} and g_F in equation 6 with parametrized density fluxes:

$$\frac{g_{dF}}{g_F} = \frac{\Delta \gamma_z S(\gamma)}{\gamma_z \Delta S(\gamma)} \quad (7)$$

where the density discretization interval is $\Delta \gamma = 0.002 \text{ kg m}^{-3}$, $\Delta \gamma_z$ and $\Delta S(\gamma)$ are equal to $(\partial \gamma_z / \partial \gamma) \Delta \gamma$ and $(\partial S / \partial \gamma) \Delta \gamma$, respectively.

In general, the vertical density gradient is highly variable along any density surface: the strongest abyssal stratification occurs near the inflow passage of the Ecuador Trench and the weakest at the incrops. The incrops are, by definition, accompanied by thick wsBBLs. Above the wsBBL, the vertical isopycnal density gradient tends to increase with decreasing densities (right panel of Figure 9). However, the profiles near the Ecuador Trench demonstrate how ocean dynamics affect the abyssal water stratification: waters just above $\gamma_{27.97}$ have weaker density gradients than below. This is because these lighter waters are part of the outflow of homogenized deep waters from the Panama Basin into the open Pacific.

Despite the tendency for the stratification in any single water column to increase with decreasing density, the basin averaged stratification does not necessarily follow this pattern. The reason for this is the incrop area, and therefore the area of weak stratification, that gradually increases for lighter abyssal waters. Large incrop areas result in a large weight of weak stratification in the basin average of $\gamma_z(\gamma)$. In the Panama Basin, the basin average of $\gamma_z(\gamma)$ varies by less than 10% at the upper boundary of abyssal wa-

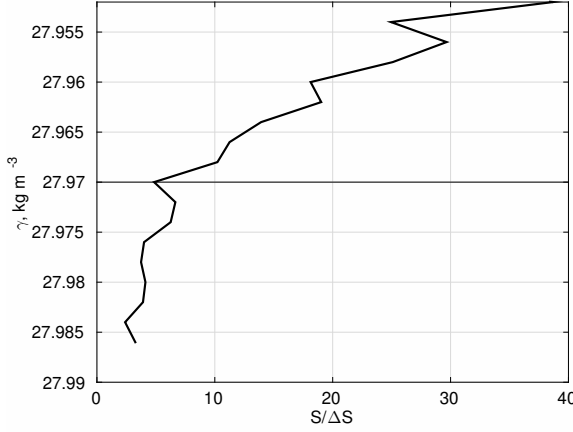


Figure 10. Ratio of the area of the isopycnal layer centred at γ to the bottom intercept area of the same layer: $S(\gamma)/\Delta S(\gamma)$, where $\Delta S(\gamma) = \frac{\partial S(\gamma)}{\partial \gamma} \Delta \gamma$ with $\Delta \gamma = 0.002 \text{ kg m}^{-3}$. The horizontal line marks the upper boundary of abyssal waters.

ter layer, in the density range between $\gamma_{27.976}$ and $\gamma_{27.970}$ (black circles in right panel of Figure 9). Furthermore, the ratio of the total isopycnal surface area (S) to the bottom intercept area (ΔS) is also exceptionally small: varying between 2 and 7 (Figure 10), due to either large ΔS , or S being much smaller than hypsometry allows it: $S < S_{max}$ (Figure 7). As a result, diabatic abyssal water upwelling at the incrops dominates over the basin-wide abyssal water upwelling ($g_{dF}/g_F < 1$).

A reverse outcome is expected for the deep waters above the abyssal water layer. The ratio S to ΔS is expected to grow significantly for deep waters controlled by hypsometry. For example, for deep waters immediately above the abyssal water layer, the $S/\Delta S$ ratio grows rapidly from an estimated value of 5 for the density layer $27.970 \pm 0.001 \text{ kg m}^{-3}$, to 40 for the isopycnal $\gamma_{27.95}$ (at $\sim 2300 \text{ m}$ depth), which is still within the semi-enclosed basin. At the same time, the basin average density gradient grows at the rate of $5 \times 10^{-6} \text{ kg m}^{-4}$ per density step of 0.002 kg m^{-3} , reaching a density gradient of $8 \times 10^{-5} \text{ kg m}^{-4}$ for the same isopycnal of $\gamma_{27.95}$ (Figure 9), resulting in the ratio of 2.5 in equation 7. The ratio is expected to increase even further with lighter waters, following the increase of ratio $S/\Delta S$. As a result, upwelling of deep (but not abyssal) waters is much more likely to be basin-wide, along the whole density surfaces, as originally suggested by Stommel [1958], unless the bottom intensified turbulence drives significant water mass transformation at the walls of the basin.

In conclusion, for abyssal waters, boundary upwelling is much more important than for the deep waters above them, because abyssal waters have access to the bottom of the basin resulting in formation of incrops and, overall, exceptionally large bottom intercept areas of density layers. This becomes even more significant when turbulence intensifies with depth, which is investigated below.

4.6 Bottom intensified mixing

To understand the turbulence driven deep water mass transformation in the basin a more realistic parametrization of turbulence must be implemented. Two scenarios are addressed here: 1) turbulent density flux is strong near the bottom and rapidly decreases with height above the bottom, 2) turbulent density flux is an order of magnitude weaker near the bottom and only slowly decreases in height. The first case represents highly turbulent regions, while the second case corresponds to ‘normal’ conditions.

Specifically, density flux is parametrized as an exponential function following *Ferrari et al. [2016]* with the reference to the global estimates of turbulent dissipation (ϵ) over ridges and rough topography [*Waterhouse et al., 2014*]:

$$F(h) = F_0 e^{-h/d}, \quad (8)$$

where F_0 is density flux at the bottom, h is height above the bottom, and d is an e-folding scale of the exponential function. However, density fluxes only above the wsBBL where considered $h > P_{wsBBL}$, because wsBBL is a layer where mixing efficiency reduces due to a very weak stratification and diffusive density fluxes at the bottom are zero.

In *Case 1*, the case of the greatest bottom intensification of turbulence, density fluxes are parametrized with parameters $F_0 = 2 \times 10^{-8} \text{ kg m}^{-2} \text{ s}^{-1}$, and $d = 500 \text{ m}$. Such a parametrization is comparable to the turbulent dissipation intensification measured over some parts of the mid-ocean ridges as given by *Waterhouse et al. [2014]*. In the case of ‘normal’ turbulence enhancement with depth (*Case 2*), density fluxes are parametrized with parameters $F_0 = 2 \times 10^{-9} \text{ kg m}^{-2} \text{ s}^{-1}$, and $d = 1000 \text{ m}$. Such parametrization is comparable to the turbulent dissipation intensification as measured over the rough topography [*Waterhouse et al., 2014*].

The water mass transformation framework used in this study is formulated in density space, hence, density fluxes expressed against the height above the bottom must be converted to density units by using the local stratification profile. Stratification profiles as a function of density (see Figure 9) are averaged on density surfaces. Thus, having a map of the bottom density, local stratification is known everywhere in the basin as well. Near the Ecuador Trench, the abyssal water source, abyssal and deep water stratification is the strongest, while over incrops it is the weakest. The largest incrops being located at the western side of the basin, the bottom intensified turbulence is much more compressed in density space at the western side of the basin, than at the eastern side.

With turbulence increasing exponentially as the bottom is approached, the largest turbulent density fluxes are found at the top of the BBL, here chosen to be P_{wsBBL} . Just above the P_{wsBBL} , the density flux convergence $\Delta F(\gamma)/\Delta\gamma$ is also at its maximum. Locally, both the density flux and its convergence decrease with lighter densities. However, the isopycnal area increases with lighter densities, which has a strong effect on area-integrated values. Consequently, the spatial integral of density flux convergence $\langle \Delta F(\gamma)/\Delta\gamma \rangle_S$ reaches a maximum just above the $\gamma_{27.970}$ (Figure 11), which has the largest incrop area.

In general, the density flux convergence is larger for those regions located over the walls of the basin. In particular, $F(\gamma)$ at the top of the wsBBL is stronger over the walls due to thin wsBBL. For example, due to variations in thickness of the wsBBL over incrops, the maximum density flux at the top of the wsBBL is on average twice smaller than the chosen F_0 value (not shown). As a second example, bottom intensified turbulence is more compressed over incrops due to weak abyssal stratification, thus, density fluxes are larger over the walls throughout the whole abyssal and deep water column. On the other hand, more compressed turbulence over the incrops means that the density flux convergence can become stronger just above the wsBBL, which explains the sharp peak in spatially integrated density flux convergence when the largest incrop area of $\gamma_{27.970}$ is included in the integration (Figure 11).

The density flux convergence drives water downwelling. The area integral of this downwelling increases for abyssal waters, reaches a maximum just above the abyssal water layer, and reduces for the deep waters above (Figure 12). The strength of the downwelling is highly sensitive to the chosen parametrization of density fluxes. With exceptionally strong bottom intensified turbulence with $F_0 = 2 \times 10^{-8} \text{ kg m}^{-2} \text{ s}^{-1}$, the largest downwelling amounts to 0.27 Sv, while upwelling at the BBL driven by the same turbulence amounts to 0.47 Sv, which yields a total upwelling at the upper boundary of abyssal wa-

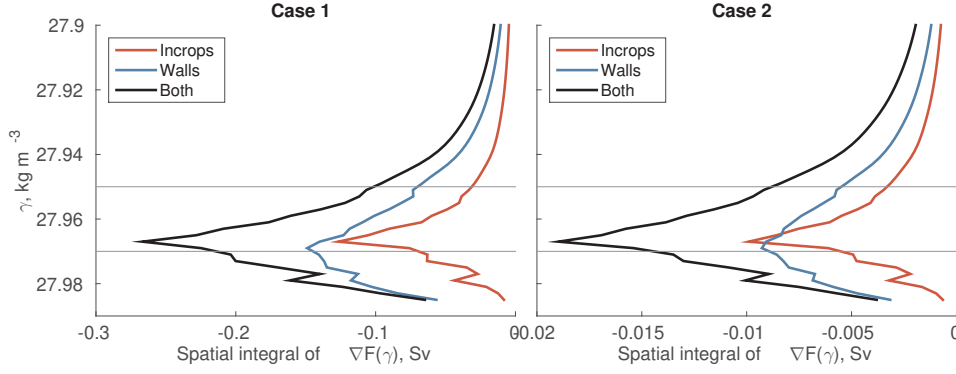


Figure 11. Spatial integral of density flux divergence above the wsBBL for the exceptionally intense bottom intensification of turbulence (*Case 1*), and for the strong bottom intensification of turbulence (*Case 2*). The integration area is divided into sections: incrops, walls of the basin, where wsBBL is very thin, and sum of both. Horizontal lines mark the upper boundary of the abyssal water layer $\gamma_{27.97}$ and the lightest isopycnal with the access to the bottom of the basin $\gamma_{27.95}$. Note the different x-axis in two figures.

ters of ~ 0.2 Sv. An order of magnitude smaller F^γ yields an order of magnitude smaller water mass transformation rates with the total upwelling estimate of ~ 0.04 Sv.

Furthermore, it is interesting to observe that in the *Case 2*, the diabatic upwelling driven by the background turbulence of constant $K_b^z = 10^{-5} \text{ m}^2 \text{ s}^{-1}$ is relatively small for abyssal waters, but as soon as density layers stop having access to the bottom of the basin, above isopycnal $\gamma_{27.950}$, the background turbulence becomes dominant. However, we note that isopycnal $\gamma_{27.950}$ spreads at depth of 2300 m, and that waters above $\gamma_{27.950}$ start to have an exchange with the tropical Pacific Basin. The incrops of those lighter waters are located outside the Panama Basin, and only a small part of their bottom intercepts are located at the walls of the Panama Basin.

In section 4.4, we have estimated that geothermal heating results in a diabatic upwelling rate across the upper boundary of abyssal water layer that has the same magnitude as the total inflow of abyssal waters into the basin of ~ 0.3 Sv. Hence, the turbulent simulation *Case 2* with very weak contribution to the total diabatic upwelling of only ~ 0.04 Sv is a more reasonable scenario than *Case 1*. All the same, *Case 2* represents a strong bottom intensification of turbulence that is comparable to the turbulent dissipation observed over rough topography [Waterhouse *et al.*, 2014].

5 Summary and Discussion

The Panama Basin serves as a conveniently small observatory for abyssal water investigation. The basin is unique in having a single passage for abyssal water inflow into the basin, the magnitude of which is estimated to be 0.29 ± 0.07 Sv [Banyte *et al.*, 2018a] and a strong geothermal heating rate inside the basin. Banyte *et al.* [2018a] estimated that about half of the densest abyssal waters inflowing through the Ecuador Trench become lighter within a distance of 200 km downstream of the sill of the trench. This study analyses how abyssal waters upwell away from the intensely turbulent narrow passage.

Together with recent studies of Ferrari *et al.* [2016]; de Lavergne *et al.* [2016]; McDougall and Ferrari [2017], we confirm that abyssal upwelling happens predominantly within the weakly stratified bottom boundary layer (wsBBL), the latter being formed when isopycnals intercept the bottom of the basin, which we denote an incrop. The incrop areas

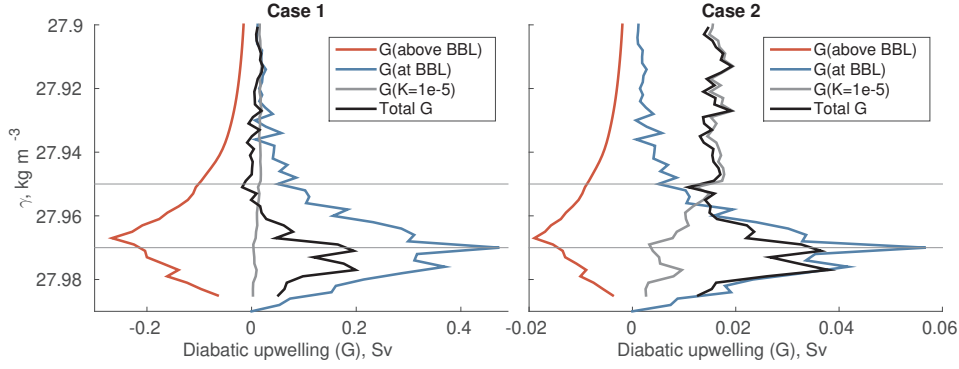


Figure 12. Spatially integrated density flux divergence in the Panama Basin for the exceptionally intense bottom intensification of turbulence (*Case 1*), and for the strong bottom intensification of turbulence (*Case 2*). The profiles show downwelling above wsBBL (red) and upwelling at the wsBBL (blue) driven by the bottom intensified turbulence, the upwelling driven by the background turbulence (gray) and their total upwelling (black). Horizontal lines mark the upper boundary of the abyssal water layer and the lightest isopycnal with the access to the bottom of the basin. Note the different x-axis in two figures.

increase as abyssal waters become lighter as they move from the eastern to the western side of the basin. Towards the west, geothermal heating also intensifies due to the presence of active spreading ridges. Large incrop areas and large geothermal heating rates result in an integral heating of bottom waters that amount to a total diabatic upwelling of 0.32 ± 0.11 Sv. Geothermal heating is the dominant forcing in the interior of the basin for abyssal water mass transformation.

Recent theories of abyssal water upwelling [Ferrari et al., 2016; McDougall and Ferrari, 2017; de Lavergne et al., 2017] are based on the assumption of a very thin (a few meters thick) bottom boundary layer, as are observed to occur in shallow waters [Moum et al., 2004]. By contrast, in the Panama Basin, the wsBBL is hundreds to over a thousand meters thick at some places. Similarly thick wsBBLs have been identified by Banyte et al. [2018b] in the global ocean. We argue that oceanic basins have the bottom surfaces, which allow thick incrops to form. The thickness of the wsBBL can be used as a rule of thumb to functionally differentiate between the oceanic bottom and its walls.

Finally, we apply a common parametrisation of the turbulence driven density fluxes to evaluate the strength of the turbulence driven upwelling at the wsBBL and of the downwelling above it. Due to the opposing effects of the exponential decrease of density fluxes with height above the bottom and a rapid rate of increase in the area of isopycnals, the maximum in the diabatic downwelling is found just above the upper boundary of the abyssal waters. Consequently, the strongest upwelling rate is estimated to occur in the lightest abyssal waters that have the largest incrop area. Nevertheless, the turbulence-driven upwelling that occurs within the wsBBL is always larger than the diabatic downwelling above the wsBBL.

In the Panama Basin, geothermal heating accounts for almost all of the water mass transformation that is required to close the abyssal water layer mass balance. From this we deduce that turbulent dissipation is responsible for only a small part of the abyssal water mass transformation. This conclusion is confirmed by application of a commonly used parametrization of turbulent density fluxes over the rough topography (Case 2, in section 4.6), which predicts just 0.04 Sv of diapycnal upwelling.

526 .1 Defining a weakly stratified bottom boundary layer

527 The vertical density gradient γ_z was computed over each 50 m with a running step
 528 of 10 m. The wsBBL was defined where the vertical density gradient was smaller than
 529 $1 \times 10^{-5} \text{ kg m}^{-4}$ and the thickness larger than 50 m. Sometimes, the water column of
 530 weak γ_z was interrupted by a short interval of high γ_z . In such cases, if the water column
 531 of weak γ_z was longer it was assumed that the part of high γ_z was an intrusion and, thus,
 532 neglected.

533 .2 Computing the incrop area

534 The γ_{wsBBL} was spatially interpolated with a nearest neighbour algorithm with 50
 535 km radius. In case of no cast found, a 150 km radius was used, instead. Then, topogra-
 536 phy that was shallower than the parametrized P_{wsBBL} of the interpolated γ_{wsBBL} was
 537 removed. To evaluate how estimated incrop areas are affected by sampling, we ran 1000
 538 simulations with 70% of all the stations randomly sampled without repetition. The full
 539 area of the γ_{wsBBL}^i surface was estimated as the horizontal area of abyssal region where
 540 densities are equal to or larger than γ_{wsBBL}^i and deeper than $P_{wsBBL}(\gamma_i)$.

541 The error of isopycnal area estimates due to sparse sampling is by far the largest.
 542 It causes the error for the incrop area estimate of $\sim 50\%$ as shown by dashed lines in
 543 Figures 6 and 8. The error of linear fit between P_{wsBBL} and γ_{wsBBL} , by comparison, is
 544 much smaller and affects incrop estimates by $\sim 5\%$. We could not assess the error caused
 545 by the geothermal heating parametrization, but assume it to be also much smaller than the
 546 sparse sampling error.

547 .3 The vertical density gradient

548 The individual vertical density profiles were grouped by their γ_{wsBBL} with dis-
 549 cretization step of 0.002 kg m^{-3} . In the range of γ_{wsBBL} chosen from 27.900 kg m^{-3}
 550 to 27.990 kg m^{-3} , in total, 45 mean vertical density profiles representing an incrop area
 551 were found. Then, each averaged profile was smoothed with a low pass filter over 400 m
 552 intervals and interpolated on a grid with 1 m increments. The basin-wide average of γ_z
 553 along neutral density surface γ was computed as:

$$554 \quad \langle \gamma_z(\gamma) \rangle = \frac{\sum_i \Delta S_I(\gamma_i) \gamma_z^i(\gamma)}{\sum_i \Delta S_I(\gamma_i)}, \quad (1)$$

554 where summation is over a number of profiles, representative of the area of the discretized
 555 incrop (ΔS_I). The basin-wide average $\langle \gamma_z \rangle$ for each density surface is marked by a
 556 black dot in Figure 9.

557 .4 Bottom intensified turbulent density fluxes

558 The turbulent density flux at the location i is computed by using formula:

$$559 \quad F^i(z) = F_0 e^{-\frac{H^i - z^i}{d}}, \quad (2)$$

560 where H^i is a local seabed depth and z^i is the depth coordinate increasing with larger
 densities as in Figure 2. Only $z^i < P_{wsBBL}^i$ was considered.

561 The spatial integration of density fluxes over each discretized incrop is carried by 1)
 562 converting $F^i(z)$ to density space ($F^i(\gamma)$), by using mean stratification profile averaged
 563 over the incrop, 2) averaging $F^i(\gamma)$ spatially over incrop area in density space with anal-
 564 ogy to equation 3, and 3) multiplying by the size of an incrop area $\Delta S_I(\gamma)$:

$$\sum_{\gamma_i < \gamma_0} \langle F(\gamma_i) \rangle |_{incrop} \Delta S_I(\gamma_i), \quad (3)$$

The spatial integration of density fluxes over bottom intercept areas of discretized density layers at the walls is carried by 1) ‘coloring’ the whole region on the walls, where ‘color’ represents the discretized bottom density in the bottom density atlas, 2) converting $F^i(z)$ to density space ($F^i(\gamma)$) depending on the ‘color’ of the location with corresponding stratification profile of the incrop, 3) averaging $F^i(\gamma)$ first over the ‘colored’ regions, than over the whole bottom intercept area at the walls, and 4) multiplying by the size of the bottom intercept area at the walls $\Delta S - \Delta S_I(\gamma)$:

$$\sum_{\gamma_i < \gamma_0} \langle F(\gamma_i) \rangle |_{walls} (\Delta S(\gamma_i) - \Delta S_I(\gamma_i)). \quad (.4)$$

The density flux divergence is integrated in a similar way. For example, over incrops, the density flux divergence for isopycnal $\gamma_0 + \frac{dy}{2}$ can be written as:

$$\sum_{\gamma_i < \gamma_0} (\langle F(\gamma_i + d\gamma) \rangle - \langle F(\gamma_i) \rangle) |_{incrop} \Delta S_I(\gamma_i). \quad (.5)$$

Acknowledgments

This Research was supported by the NERC OSCAR project grants NE/I022868/2 (Morales Maqueda, 2015) and NE/I027010/1 (Hobbs, 2015). The authors would like to thank the officers, crew, technicians and science party on board the RRS James Cook during cruises JC112, JC113 and JC114 and R/V Sonne during cruise SO238. We are grateful to the Alvaro Morales Ramírez (Centro de Investigación en Ciencias del Mar y Limnología, Universidad de Costa Rica), Nancy Villegas Bolanos (Departamento de Geociencias, Universidad Nacional de Colombia) and Galo Quezada (Reserva Marina de Galápagos) for their invaluable help during the OSCAR project fieldwork. We also thank the “Ministerio de Ambiente y Energía”, Costa Rica, the Armada de la República de Colombia, and the Instituto Oceanográfico de la Armada de Ecuador (INOCAR) for the support provided to the said fieldwork. The data from this campaign are made available through the British Oceanographic Data Centre (bodc.ac.uk).

References

- Adcroft, A., Scott, J. R., and Marotzke, J. (2001). Impact of geothermal heating on the global ocean circulation, *Geophys. Res. Lett.* 28, 1735–1738
- Amante, C. and Eatkins, B. W. (2009). ETOPO1 1 Arc-Minute Global Relief Model: Procedures, Data Sources and Analysis. NOAA Technical Memorandum NESDIS NGDC-24, *National Geophysical Data Center, NOAA*, doi:10.7289/V5C8276M
- Banyte, D., Morales Maqueda, M. A., Hobbs, R., Smeed, D., and Megann, A. (2018). Geothermal heating in the Panama Basin. Part I: hydrography of the basin, *J. Geophys. Res.* submitted
- Banyte, D., Smeed, D., and Morales Maqueda, M. A. (2018). The Weakly Stratified Bottom Boundary Layer of the Global Ocean, *J. Geophys. Res.*, doi:10.1029/2018JC013754
- de Lavergne, C., Madec, G., le Sommer, J., Nurser, A. J. G., and Garabato, A. C. N. (2016). On the Consumption of Antarctic Bottom Water in the Abyssal Ocean, *J. Phys. Oceanogr.* 46, 635–661
- de Lavergne, C., Madec, G., Roquet, F., Holmes, R. M., and McDougall, T. J. (2017). Abyssal ocean overturning shaped by seafloor distribution, *Nature* 551, 181–186.
- Emile-Geay, J. and Madec, G. (2009). Geothermal heating, diapycnal mixing and the abyssal circulation, *Ocean Sci.* 5, 203–217
- Ferrari, R., Mashayek, A., McDougall, T. J., Nikurashin, M., and Campin, J. M. (2016). Turning ocean mixing upside down, *J. Phys. Oceanogr.* DOI: <http://dx.doi.org/10.1175/JPO-D-15-0244.1>.

- Ledwell, J. R., Montgomery, E. T., Polzin, K. L., St. Laurent, L. C., Schmitt, R. W., and Toole, J. M. (2000). Evidence for enhanced mixing over rough topography in the abyssal ocean, *Nature* 403, 179–182.
- Hofmann, M. and Morales Maqueda, M. A. (2009). Geothermal heat flux and its influence on the oceanic abyssal circulation and radiocarbon distribution, *Geophys. Res. Lett.* 36, L03603
- Jackett, D. R. and McDougall, T. J. (1997). A neutral density variable for the world's oceans, *J. Phys. Oceanogr.* 27, 237–263.
- Klocker, A. and McDougall, T. J. (2010). Influence of the Nonlinear Equation of State on Global Estimates of Dineutral Advection and Diffusion, *J. Phys. Oceanogr.* 40, 1690–1709, doi: 10.1175/2010JPO4303.1.
- Mantyla, A. W. and Reid, J. L. (1983). Abyssal characteristics of the World Ocean waters, *Deep Sea Res.* 30(8), 805–833
- McDougall, T. J. and Ferrari, R. (2017). Abyssal Upwelling and Downwelling Driven by Near-Boundary Mixing, *J. Phys. Oceanogr.* 47, 261–283.
- Moum, J. N., Perlin, A., Klymak, J. M., Levine, M. D., Boyd, T., and Kosro, P. M. (2004). Convectively Driven Mixing in the Bottom Boundary Layer, *J. Phys. Oceanogr.* 34, 2189–2202.
- Müller, R. D., Roest, W. R., Royer, J. Y., Gahagan, L. M., and Sclater, J. G. (1997). Digital isochrons of the world's ocean floor, *J. Geophys. Res.* 102, 3211–3214
- Munk, W. H. (1966). Abyssal recipes, *Deep Sea Res. and Oceanogr. Abstr.* 13, 707–730
- Nurser, A. J. G., Marsh, R., and Williams, R. G. (1999). Diagnosing Water Mass Formation from Air–Sea Fluxes and Surface Mixing, *J. Phys. Oceanogr.* 29, 1468–1487
- Polzin, K. L., Toole, J. M., Ledwell, J. R., and Schmitt, R. W. (1997). Spatial Variability of Turbulent Mixing in the Abyssal Ocean, *Science* 276, 93–96.
- Stein, C. A. and Stein, S. (1992). A model for the global variation in oceanic depth and heat flow with lithospheric age, *Nature* 359, 123–129
- St. Laurent, L. C., Toole, J. M., and Schmitt, R. W. (2001). Buoyancy Forcing by Turbulence above Rough Topography in the Abyssal Brazil Basin, *J. Phys. Oceanogr.* 31, 3476–3495.
- Stommel, H. (1958). The abyssal circulation. Letter to the editors, *Deep Sea Res.* 5, 80–82
- Walín, G. (1982). On the relation between sea-surface heat flow and thermal circulation in the ocean, *Tellus* 34, 187–195.
- Waterhouse, A. F., MacKinnon, J. A., Nash, J. D., Alford, M. H., Kunze, E., Simmons, H. L., Polzin, K. L., St. Laurent, L. C., Sun, O. M., Pinkel, R., Talley, L. D., Whalen, C. B., Huussen, T. N., Carter, G. S., Fer, I., Waterman, S., Naveira Garabato, A. C., Sanford, T. B., and Lee, C. M. (2014). Global Patterns of Diapycnal Mixing from Measurements of the Turbulent Dissipation Rate, *J. Phys. Oceanogr.* 44, 1854–1872